



# Graphene/TiO<sub>2</sub> based photo-catalysts on nanostructured membranes as a potential active filter media for methanol gas-phase degradation

M. Roso\*, A. Lorenzetti, C. Boaretti, D. Hrelja, M. Modesti\*

University of Padova Department of Industrial Engineering, Via Marzolo, 9, 35131 Padova, Italy

## ARTICLE INFO

### Article history:

Received 8 January 2015  
Received in revised form 16 March 2015  
Accepted 3 April 2015  
Available online 4 April 2015

### Keywords:

Graphene  
Nanostructured membranes  
Methanol gas-phase photo-degradation  
Titanium dioxide  
Nanofibers

## ABSTRACT

Photocatalytic oxidation processes (PCO) represent more and more promising technologies for air purification and the development of new solutions in pollution sensing and prevention by using adequate nanostructures with unique properties has gained more interest in the scientific community. The present work is meant to show the production, characterization and the photocatalytic performance of nanostructured membranes based on electrospun polyacrylonitrile (PAN) scaffolds and graphene/titania based catalysts. Three different systems of photocatalyst were chosen in order to compare their photocatalytic properties: pristine TiO<sub>2</sub>, TiO<sub>2</sub> plus a few-layers graphene and TiO<sub>2</sub>/reduced-graphene composite obtained by hydrothermal method from graphene oxide. Results of the photocatalytic performance on methanol gas-phase degradation, revealed a higher reaction rate of the graphene based photocatalysts wherein an effective charge transfer, enhanced by graphene, has been supposed to reduce the charge recombination increasing the photocatalytic activity of TiO<sub>2</sub> nanoparticles. Moreover, it has been found that the performance of the nanostructured membranes can be restored by stripping with an inert gas several times and this property makes them a good candidate as active filter media.

© 2015 Elsevier B.V. All rights reserved.

## 1. Introduction

Smog hanging over cities is the most familiar and obvious form of air pollution. But there are different kinds of pollution and we all are subjected to both outdoor and indoor pollutants. Since the outdoor air quality has become a growing concern as modern industrialization begun, the monitoring of outdoor air pollution has become more and more systematic in western countries. On the contrary, the indoor air quality is still not regulated by national or international legislation but the World Health Organization released in 2010 a guidelines text as an assessment of effectiveness of policies protecting against harmful exposure to chemical and biological indoor pollutants [1]. Among indoor air pollutants, Volatile Organic Compounds (VOCs) represent well-known chemicals, which are strongly involved in a wide range of industrial processes and because of their intrinsic properties, they pass through the final products the people get in contact with. In summary, alcohols, aromatics, aldehydes and halocarbons are just few classes of VOCs which are emitted from several sources, such as construction coverings, household cleaning products, furnitures,

paints..to cite some examples. The reader can find in the literature [2] an exhaustive review on VOCs in indoor environment. According to our previous work [3], photocatalytic oxidation have been proven to be a promising technology for air purification and nanostructured membrane based on electrospun nanofibers offer a proper support in the production of active filtering media which combine the physical activity with the chemical degradation of harmful pollutants.

Among carbon nanomaterials (e.g., fullerenes (C60), carbon nanotubes (CNT), carbon nanofibers, nanodiamond) graphene is attracting widespread attention because its sp<sup>2</sup>-hybridized two-dimensional carbon structure, results on a better thermal conductivity (5300 W/mK), charge carrier mobility (~2000 S/cm), and larger surface area (~2630 m<sup>2</sup>/g) than unrolled CNT [4]. According to Engineering Village search engine, the published articles on graphene jumped from 2765 in 2010 to 8832 in 2013, by means that the scientific community has recognized the great potential of graphene and graphene composites in a wide range of applications, such as photocatalysis [5–9], lithiumion batteries [11,12], and solar cells [13–15]. As regards the photocatalytic applications of graphene, Khalid et. al [5] reported an hydrothermal method to prepare TiO<sub>2</sub>-graphene composites, while Kim et al. [7], on the other side, tested the photocatalytic performance of carbon nanofibers loaded with TiO<sub>2</sub> nanoparticles and graphene. In both

\* Corresponding authors. Tel.: +39 498275735.

E-mail addresses: [martina.roso@unipd.it](mailto:martina.roso@unipd.it) (M. Roso), [michele.modesti@unipd.it](mailto:michele.modesti@unipd.it) (M. Modesti).

cases organic dyes are used as a model substrate in order to evaluate the photo-oxidation performance of the catalytic system. There is just a scientific paper to our knowledge, [10], which deals with a comparative study of the photocatalytic properties of the heterostructures produced by impregnation of TiO<sub>2</sub> by graphene oxide on ethanol and benzene gas-phase oxidation. The added value of the present work is related to the comparative study of the photocatalytic performance of three different photo-catalytic systems, based on TiO<sub>2</sub>, TiO<sub>2</sub> and graphene and a nanocomposite TiO<sub>2</sub>/rGO with respect the gas phase degradation of methanol.

## 2. Experimental

### 2.1. Materials

The graphene used in this study as co-photocatalyst was avanGraphene (1–2 layers) produced by Avanzare Innovacion Tecnologica S.L. (La Rioja) Spain.

The reduced GO (rGO)-TiO<sub>2</sub> composite was synthesized according to Khalid et al. [5] by a simple hydrothermal method. Briefly, 20 mg of Graphene Oxide sheets (GO, Sigma–Aldrich, USA) were dispersed in a solution of distilled water (80 mL) and ethanol (40 mL) mixture using ultrasonic mixing for 2 h, and then 200 mg of TiO<sub>2</sub> (Aeroxide® P25, TiO<sub>2</sub> purchased from Evonik industries) were added to the obtained GO stable dispersion and stirred for another 2 h to get a homogeneous suspension. The suspension was then placed in a 200 mL Teflon-sealed autoclave and maintained at 120 °C for 3 h to attain both the reduction of GO and the deposition of TiO<sub>2</sub> on graphene sheets. Finally, the resulting composite was recovered by filtration, rinsed by deionized water several times, and dried at 70 °C for 12 h. The obtained composite photocatalyst had a weight ratio rGO /TiO<sub>2</sub> equal to 1:10.

Polyacrylonitrile (PAN, Mw 150,000 Dalton purchased from Sigma–Aldrich, USA) has been chosen as a polymer for nanofibers production thanks to its high UV resistance and N,N-dimethylformamide (DMF, from Sigma–Aldrich, USA) was used as a solvent after dehydration by storage over molecular sieves. Two dispersant agents, Dynasylan® 4144 (Evonik–Degussa) and sodium dodecyl sulfate, SDS, (Sigma–Aldrich, USA), were added at the TiO<sub>2</sub> nanoparticles and graphene suspensions, respectively, in order to improve the suspension stability.

### 2.2. Membranes production

According to the methodology previously published [3], a 5%wt solution of PAN in N,N-dimethylformamide had been produced and then electrospun on a rotating collector. After a suitable amount of fibres had been collected, electrospinning was stopped and electro-spraying of the proper catalytic system suspension was performed. Three different kind of membranes had been obtained varying the photocatalyst/co-photocatalyst system spread over the nanofibers surface according to the outline presented in Fig. 1, wherein all the steps involved during each membrane type production are reported. The details of the electro-sprayed suspensions are the following:

- TiO<sub>2</sub>, 5% w/w in ethanol, 40 min ultrasonication (Vibracell 200 W, amplitude 40%) and dispersant agent addition, according to [16].
- Few-layer graphene suspension 0.25% w/w in ethanol, 20 min ultrasonication, addition of 1% w/w of SDS with respect the solvent weight, followed by 15 min sonication.
- TiO<sub>2</sub>/graphene nanocomposite suspension, obtained by the aforementioned hydrothermal method, properly stabilized by dispersant agent addition (1% w/w SDS).

**Table 1**

Operating conditions optimized for all the electro-sprayed suspension at fixed Voltage (15 kV) and with a distance between electrodes of 12 cm.

Electro-sprayed suspension	Flow rate [ml/h]	Time [min]
TiO <sub>2</sub>	8	14
Graphene	4.5	6
Nanocomposite TiO <sub>2</sub> /graphene	6	40

The optimized conditions for all the deposition processes are shown in Table 1.

For the sake of clarity, in the present work, all the tested membranes will be named as Type A, Type B and Type C referring to the nanostructured membrane with pristine TiO<sub>2</sub>, the multilayered membrane based on graphene and TiO<sub>2</sub> and the nanocomposite one with the TiO<sub>2</sub>/graphene catalytic system, respectively. Moreover, in order to evaluate the effect of graphene content, membrane Type B were also prepared by increasing the deposition time of graphene suspension, in order to double the amount of co-photocatalyst (verified by gravimetric method). This membrane will be named as Type B-2. Each membrane Type, the images of which are presented in Fig. 2, were stored overnight in a vacuum chamber for drying and solvent stripping. The amount of photocatalyst has been expressed in terms of mg of photocatalyst per cm<sup>2</sup> of membrane.

### 2.3. Methods

As regards the characterization methods, scanning electron microscopy, SEM, (JSM-6490, JEOL Ltd., Japan) and transmission electron microscopy, TEM, (FEI Tecnai G12, 100KV with TVIPS Tietz F114 photocamera) were used for morphological analysis. Sample preparation for TEM imaging had been carried out as follows: the membrane samples were embedded in a proper epoxy resin and slices of 100 nm thickness were obtained by ultramicrotomy of the cured resin. In order to verify the reduction of GO to rGO in the nanocomposite membranes, Wide Angle X-ray diffraction (WAXD) patterns were recorded in a 2 $\theta$  angular range of 1.5° to 40° on a Philips X'Pert PRO diffractometer, working in reflection geometry and equipped with a graphite monochromator on the diffracted beam (CuK $\alpha$  radiation). The scanning step size was 0.02° with a measured uncertainty in terms of *d*-spacings of about 0.05 nm (2 $\sigma$ ). Thermogravimetric analysis (TGA, SDT-Q600 TA Instruments) have been employed for evaluating the photocatalyst content.

The surface chemistry of the materials in terms of crystal structure, disorder and defects has been explored by Raman spectroscopy (Micro Raman DRX, Thermofisher) using a laser excitation wavelength of 532 nm and 0.5 mW laser to preserve sample from damaging or laser induced heating, using 100  $\times$  objective.

The photoreactor (a Pyrex tubular reactor of 370 mm length, 100 mm of internal diameter and a volume of 2780 cm<sup>3</sup>) and the experimental set up adopted in this study had been presented in a previous work [3]. However, in this work the mode of air flow enrichment in the pollutant has been changed. Briefly, according to the experimental set up scheme in Fig. 3 the inlet gas stream, controlled by a mass flow controller for gas (Bronkhorst® High-Tech, The Netherlands) was brushing a saturator containing the organic compound. Before starting experiments, which were performed in discontinuous mode, the batch reactor was flushed with methanol/air mixture at 155 cm<sup>3</sup>/min for two hours for conditioning the system. Once the concentration of VOCs was stabilized, the valves of the photoreactor were closed, the UV lamp was turned on and the concentration of VOCs was recorded with the reaction time throughout the test. Sampled VOCs were injected through a six-port external injection GC valve (6890 Valco Instrument Co., Inc.,) with a 2 ml sample loop. The samples were then transferred to a gas chromatograph HP G1800C GCD series II GC/MS with pure

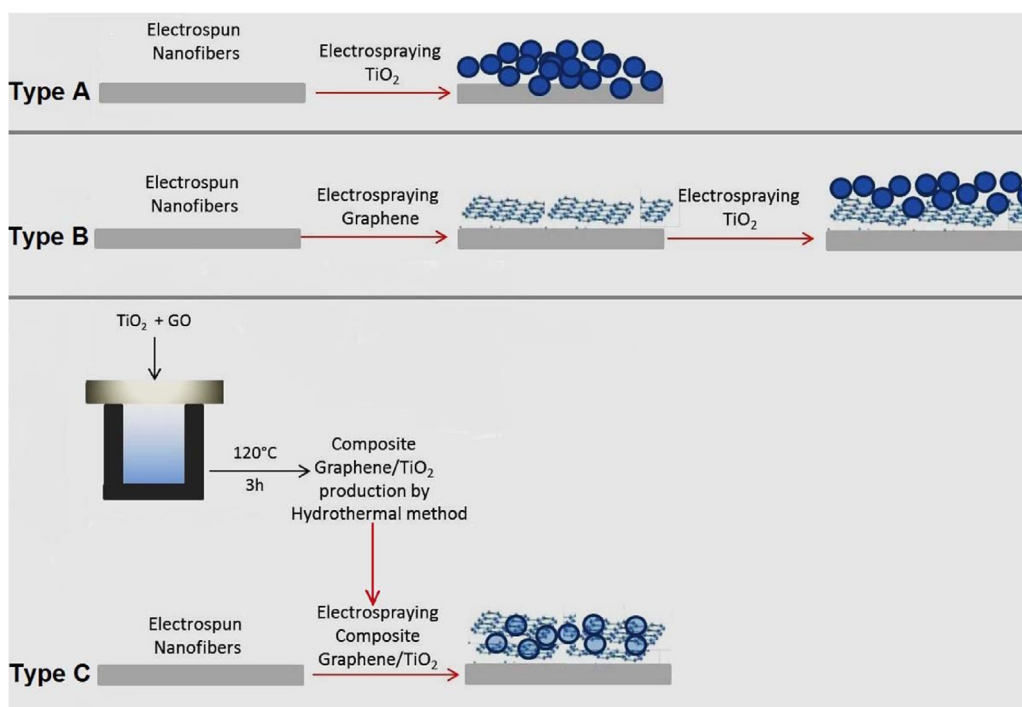


**Fig. 1.** Outline of the membrane production steps: Type A, PAN nanofibers and pristine  $\text{TiO}_2$  nanoparticles; Type B, multilayered PAN nanofibers, graphene layer and  $\text{TiO}_2$  nanoparticles; Type C, PAN nanofibers and  $\text{TiO}_2$ /graphene composite.

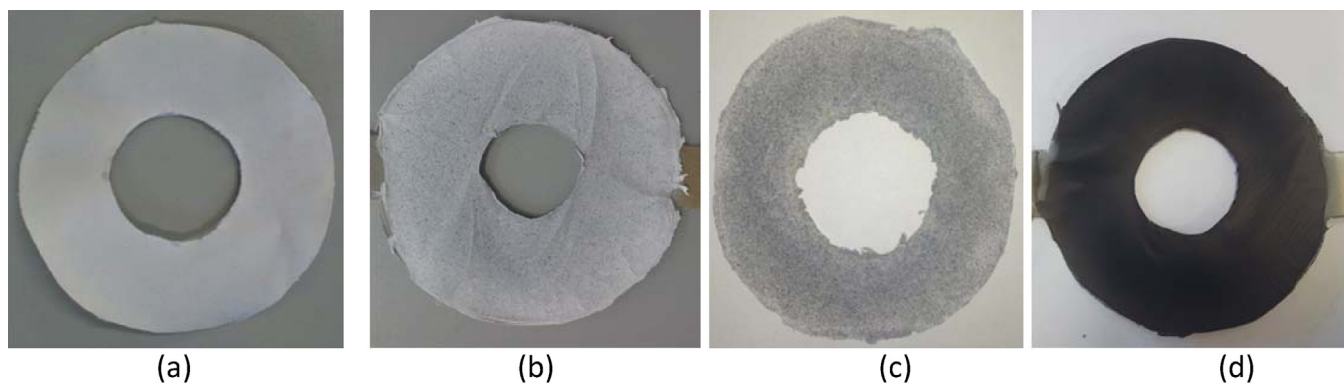


**Fig. 2.** Images of the nanostructured membranes (a) Type A; (b) Type B; (c) Type B-2; (d) Type C.

helium as a carrier gas and with a capillary column MEGA (0.32 i.d., 30 m length and 5  $\mu\text{m}$  thickness).

#### 2.4. Photocatalytic experimental set up

The photocatalytic activities of the nanostructured membranes (Type A–C) were investigated by a gas-phase analysis of the degradation of methanol under UV illumination (Fig. 3).

The initial concentration has been evaluated working on a calibration curve where the vapor fractions of methanol at different temperatures were evaluated by Rault–Dalton's law [3], and it is in perfect agreement with the concentration calculated by Eq. (1) for steady-state diffusion of one gas through a second stagnant gas [17]:

$$N_{A,z} = \frac{cD_{AB}}{Z_2 - Z_1} \ln \frac{(1 - y_{A2})}{(1 - y_{A1})} \quad (1)$$

where  $N_{A,z}$  is the constant molar flux of A (methanol),  $c$  is the total molar concentration of gas,  $D_{AB}$  is the coefficient of diffusion of

methanol (A) in air (B),  $D_{AB} = 1.5 \times 10^{-5} \text{ m}^2/\text{s}$ ,  $z_2 - z_1$  is the difference between the level of air inlet and the level of pure liquid (Fig. 3),  $y_{A2}$  is the vapor fraction of methanol at  $z_2$ , set  $y_{A2} = 0$  and  $y_{A1}$  is the equilibrium vapor fraction of methanol at  $T = 0^\circ\text{C}$ . The resulting molar fraction of methanol in the inlet air stream was then calculated to be 3100 ppm.

This assumption is related to the experimental set up chosen in this work, wherein the narrow tube of uniform cross section is partially filled with pure liquid A (methanol) and it is maintained at a constant temperature ( $T = 0^\circ\text{C}$ ) and pressure. Gas B (air), flows across the open of the tube, and it has a negligible solubility in liquid A, as well as it is also chemically inert to A. (i.e., no reaction between A and B). Component A vaporizes and diffuses into the gas phase; the rate of vaporization may be physically measured and may also be mathematically expressed in terms of the molar flux. Consider the control volume  $S \Delta z$ , where  $S$  is the cross sectional area of the tube, the mass balance on A over this control volume for a steady-state operation yields Eq. (1).

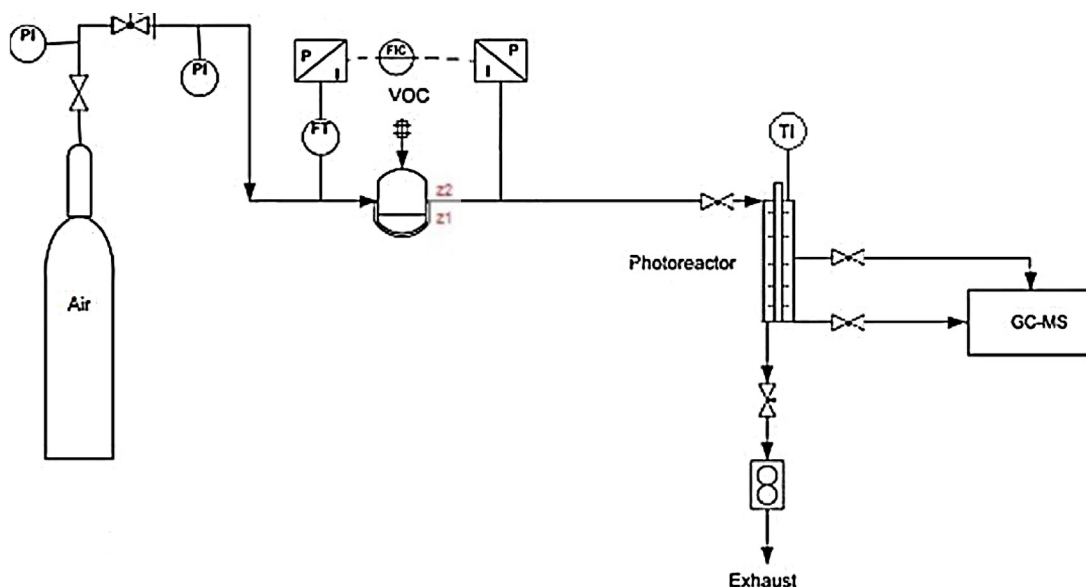


Fig. 3. Schematic diagram of catalyst performance test system.

### 3. Results and discussion

#### 3.1. Materials and membranes characterization

Before membrane production, both avanGraphene and Graphene Oxide sheets were characterized by Raman spectroscopy in order to evaluate their quality [18–21]. The Raman spectra are reported in the Supplementary file. As regards avanGraphene (Fig. S1), the characteristic D band peak was observed at  $1344\text{ cm}^{-1}$ , the G band peak at  $1590\text{ cm}^{-1}$ , the 2D band peak at  $2688\text{ cm}^{-1}$ , and it has been also revealed the not very common D+G band at  $2923\text{ cm}^{-1}$ . By looking at the position of the 2D band, AvanGraphene was assessed to be a few-layer graphene, characterized by the presence of several defects (high D band absorbance). The Raman spectra of GO and r-GO-TiO<sub>2</sub> nanocomposite after hydrothermal methods are also reported in Fig. S1, and they show strong D (at  $1345\text{ cm}^{-1}$ ) and G (at  $\sim 1590\text{ cm}^{-1}$ ) peaks, suggesting very small crystal sizes [22]. In addition,  $I_D/I_G$  ratio was used to measure structural disorder which was slightly decreased from 1.05 to 1.02 probably because of the decrease in the  $\text{sp}^2$  domain size of carbon atoms and the reduction of  $\text{sp}^3$  to  $\text{sp}^2$  carbon during the hydro thermal process [23]. Moreover in the r-GO-TiO<sub>2</sub> spectrum the anatase phase exhibits peaks at 146, 397, 518, and  $639\text{ cm}^{-1}$  [24].

All the produced membranes were characterized by SEM analysis in order to have a better understanding of the morphology variation after every single step of deposition (see Fig. 1). The micrographs of the membranes had been reported in Figs. 4 and 5: as it can be observed, the TiO<sub>2</sub> nanoparticles had the tendency to create clusters when spread over the nanofibers surface (Fig. 4). Looking at the membrane Type B, in Fig. 5a it had been shown a micrograph of the electrospun PAN sample after graphene deposition: the graphene sheets created some areas wherein a smooth surface was evident and it can be observed that the nanofibers are still visible underneath the thin layer of graphene. In the subsequent step of TiO<sub>2</sub> deposition, the nanoparticles spread over these areas appeared with a more uniform distribution and large areas wherein they are arranged (Fig. 5b) side by side were present (Fig. 5b at high mag). Membrane Type B-2 revealed a larger surface covered by graphene sheets (Fig. 5c), but the TiO<sub>2</sub> layer has been shown to be similar to membrane Type B (see Supplementary information file, Fig. S3). As regards membrane Type C,

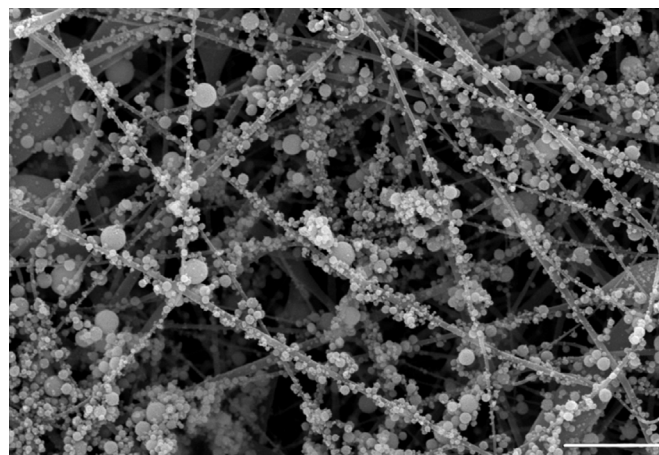


Fig. 4. SEM micrograph of membrane Type A (bar scale 10 m).

the SEM micrographs (Supplementary information file, Fig. S4) did not show morphological difference in terms of deposition, with respect the typical behavior of TiO<sub>2</sub> nanoparticles, since the TiO<sub>2</sub>/graphene composite had the same tendency to create cluster over the nanofibers. The morphological difference among the membranes were better appreciated by performing TEM analysis. Fig. 6 and Fig. 7 show the comparison of the TEM images of membrane Type B and Type C. In membrane Type B (Fig. 6) all the components were evident: the outer layer of TiO<sub>2</sub> nanoparticles, the underneath graphene sheets, and the nanofibers cross section (the spherical shapes within the gray matrix). On the contrary, looking at the TEM images of membrane Type C (Fig. 7), it was not possible to distinguish all the components at low magnification (Fig. 7a), but it was clear at higher magnification, as the graphene resulted completely embedded within the TiO<sub>2</sub> nanoparticles.

According to the results obtained in the literature [25,26], in order to verify that the hydrothermal process resulted in the partial graphene oxide reduction to reduced-GO, WAXD patterns were analyzed to test the effectiveness of such treatment. The WAXD pattern of the as-prepared TiO<sub>2</sub>-graphene composites is shown in Fig. 8.

The peaks at  $2\theta$  values of 25.3, 37.8, 48.0, 53.9, 55.1, 62.7, 68.8, 70.3, and  $75.0^\circ$  can be indexed to (101), (004), (200), (105),



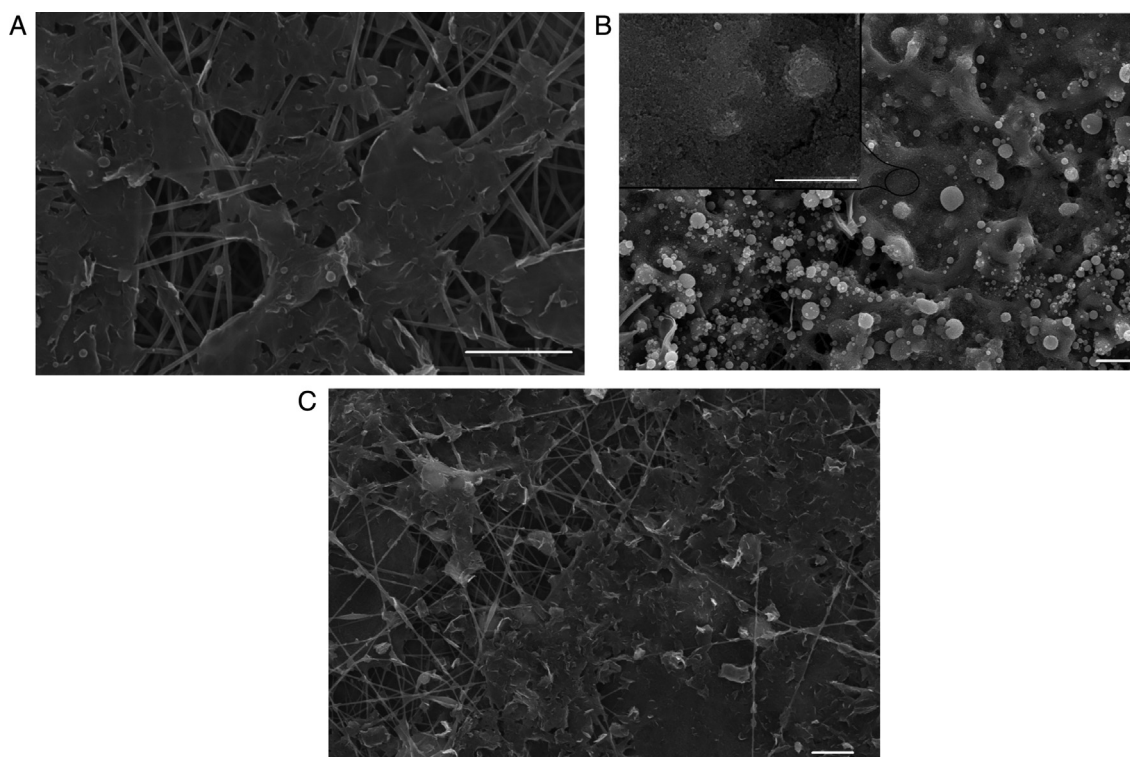


**Fig. 5.** SEM Micrograph of membrane Type B;(a) graphene layer electrospayed over electrospun nanofibers (bar scale 5 m);(b) TiO<sub>2</sub> nanoparticles spread over graphene layer (bar scale 10 m) and in the left corner higher magnification (bar scale 5 m); (c) micrograph of membrane Type B-2 graphene layer.

**Table 2**

Catalyst content calculated by TGA residual weight.

Membrane type	TiO <sub>2</sub> content (mg/cm <sup>2</sup> )
Type A	0,60 ± 0,01
Type B and B-2	0,37 ± 0,01
Type C	0,55 ± 0,01

(2 1 1), (2 0 4), (1 1 6), (2 2 0), and (2 1 5) crystal planes of anatase TiO<sub>2</sub> in P25, respectively. In addition, characteristic diffraction peaks at 27.4, 36.1, and 41.2° are also observed, which are attributed to the (1 1 0), (1 0 1), and (1 1 1) faces of rutile TiO<sub>2</sub> in P25. Notably, the typical diffraction peak of GO at  $2\theta = 14.1\text{--}14.9^\circ$  [25] is not present in the recorded pattern, meaning an effective reduction of GO to a few layer-graphene. On the other side, the diffraction peaks belonging to the separate graphene were not observed in the nanocomposites. The reason can be ascribed to the fact that the main characteristic peak of graphene at 26.28 [25,26] might be shielded by the main peak of anatase TiO<sub>2</sub> at 25.4°.

The photocatalyst content and its uniform distribution on the membranes were arisen from Thermogravimetric analysis. Each membrane type was cut in two pieces, and the related TGA analysis were performed in oxidative atmosphere (air). From the thermograms (see Supplementary information file) it can be depicted that the residual weight % which is representative of the only photocatalyst content, was ranging between 47–55% (Fig. S5), 45% (Fig. S6) and 41–43% (Fig. S7) for membrane Type A, Type B and Type C, respectively. These values and their small variation, allowed the assumption that the photocatalyst is well distributed over the membrane. The photocatalyst content for each membrane type is summarized in Table 2. Moreover the same analysis were carried out both before and after use, resulting in a negligible variation in the content within the error of the instrument. This reflects the stability of TiO<sub>2</sub> nanoparticles which adhered to the nanofibers surface thanks to Van der Waals forces, which have been demonstrated

before [3] to have a strong effect on its microscopic and macroscopic behavior, leading to agglomeration and adhesion to the surface.

### 3.2. Photocatalytic performance

The photocatalytic degradation of methanol has been studied in discontinuous mode for all the nanostructured membranes, in order to compare the catalytic performance and to evaluate the effect of graphene on the kinetic of reaction. Blank experiments at the same conditions shown that no activity is observed in the absence of photocatalyst or light irradiation. All the experiments were replicated on three sets of each membrane type, for statistical significance and three consecutive cycles of photo-degradation have been run for all the membranes, in order to estimate the lifetime of these active filter media. Every cycle consists of a conditioning step, a reaction step and a regenerative step. Fig. 9 reports the comparison of methanol photo-degradation during the experiment time (fixed at 300 min) of all the nanostructured membranes, that is Type A (pristine TiO<sub>2</sub> as photocatalyst), Type B (with the co-photocatalyst graphene), and Type C (with the composite photocatalytic system graphene-TiO<sub>2</sub>), with respect the initial concentration. As it can be observed for membrane Type A, at the beginning of the experiment, which correspond to the lighting of the UV lamp, an increase of methanol concentration has been recorded. This behavior has been hypothesized to be related to methanol-desorption, which is predominant to degradation in the first stage of the photocatalytic reaction. After the first sampling, the reaction the methanol degradation was observed and the maximum conversion reached after 300 min of experiment was 80%.

Several kinetic models have been published in literature [27], but none of them could completely account for all possible variables affecting the degradation rate. Moreover, owing to the complex mechanism of reactions, it is difficult to develop a model for the dependence of the photocatalytic degradation rate on the experimental parameters for the whole treatment time

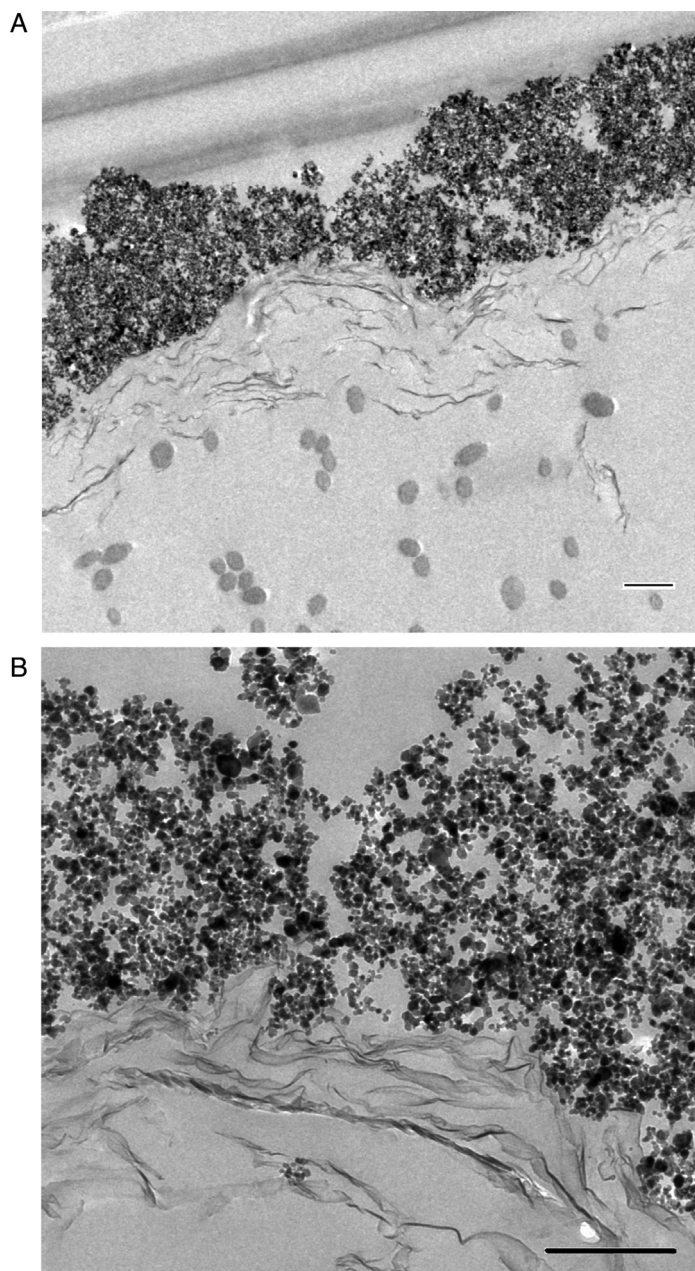


**Fig. 6.** TEM micrographs of membrane Type B at different magnification (bar scale 500 nm).

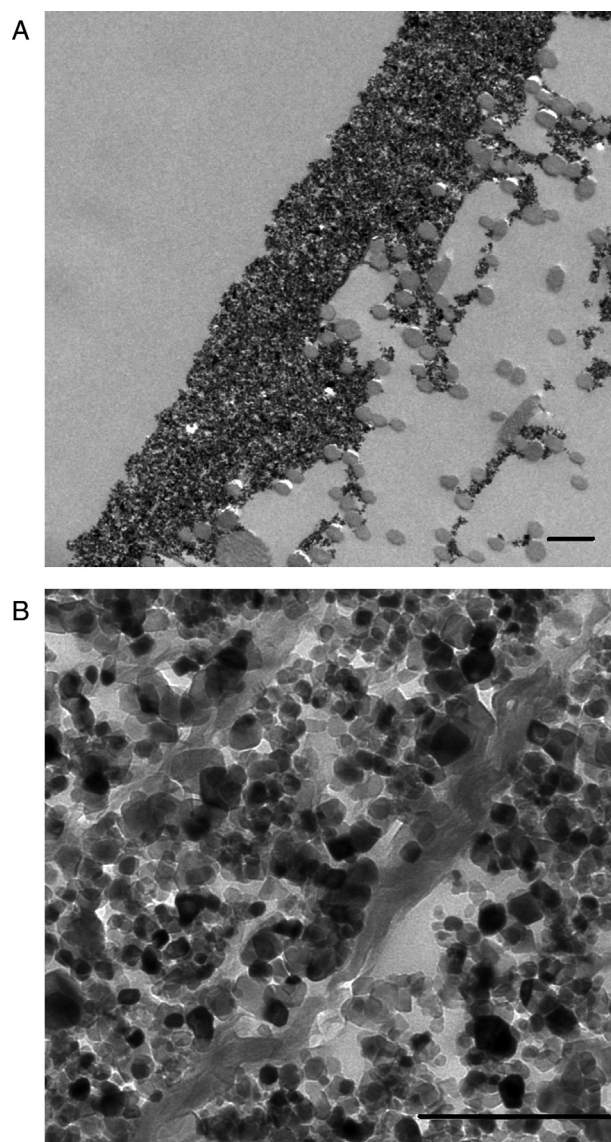


**Fig. 7.** TEM micrographs of membrane Type C at different magnification: (a) (bar scale 500 nm), (b) (bar scale 250 nm).

as well as the assumption of monomolecular adsorption of the Langmuir–Hinshelwood (L–H) model [28] is too restrictive for this catalytic scenario. Thus, in order to analyze the experimental data, the integral method for batch reactor has been implemented [29]. The kinetic constants obtained from the linearization of the kinetic curves (Fig. 10) for membrane Type B and C, have been found to be  $k = 0,04 \text{ min}^{-1}$  and  $k = 0,03 \text{ min}^{-1}$ , respectively, assuming a first

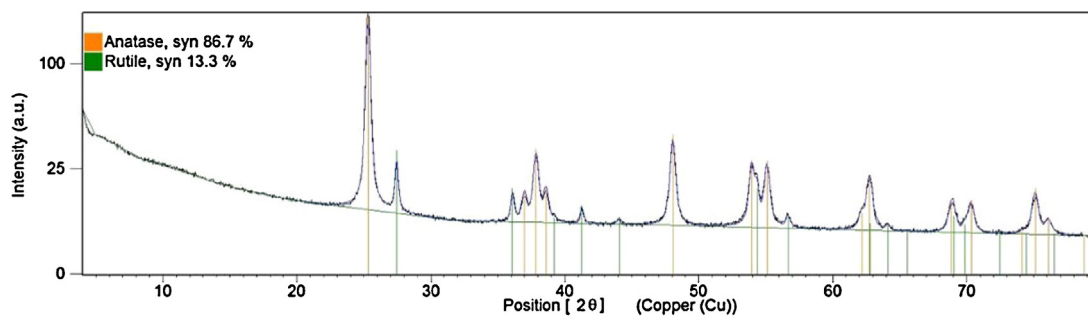


**Fig. 8.** WAXD pattern of the as-prepared  $\text{TiO}_2$ -graphene composite.



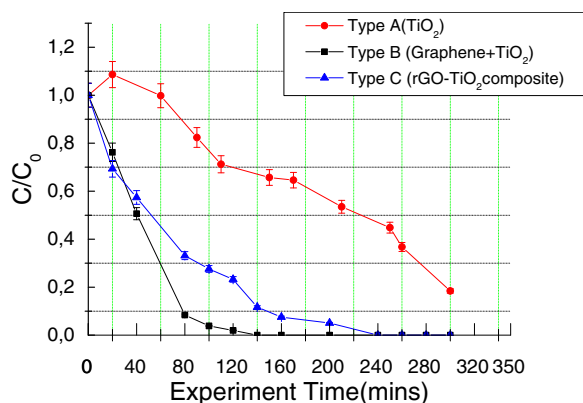


Fig. 9. Plot of the ratio  $C/C_0$  vs time for different nanostructured membranes.

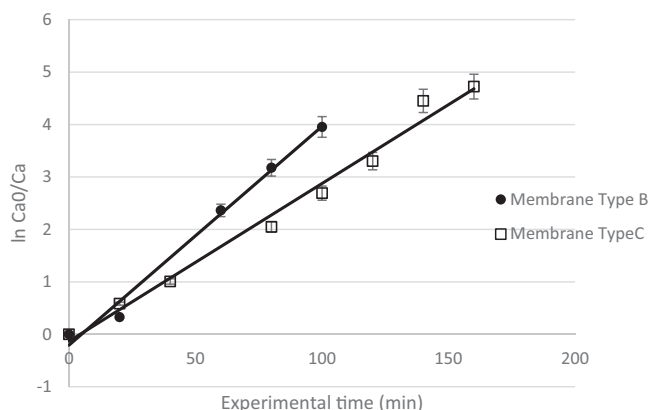


Fig. 10. Plot of the first order kinetic for the membranes Type B and Type C.

order kinetics ( $R^2 = 0.9884$  for Type B and  $R^2 = 0.9865$  for Type C). These values show a different rate observed for the tested membranes, Type B and Type C, respectively. In fact from Fig. 9 it can be observed that for both the graphene based membranes (Type B and Type C) a complete conversion has been reached. The only difference between the activity of the two nanostructured membranes is the reaction rate in an intermediate region of time, by means that methanol degradation was completed on membrane Type B in a shorter time than nanocomposite membrane (Type C). Further evidence of this behavior can be depicted from the analysis of the reacted moles for gram of photocatalyst calculated for all the membrane types. The values are summarized in Table 3 and it has been demonstrated that the number of moles reacted per gram of photocatalyst are generally higher in the layer-by-layer membrane (Type B). This behavior is not easy to understand at all, because to the author's knowledge there are not similar studies in the literature. However it has been speculated that such performance could be related to the different structural distribution of graphene. In the layer by layer membranes, there is an evident graphene layer which cover all the membrane itself, forming a conductive network, able to promote the charge transfer during the experiment.

**Table 3**  
Moles reacted for gram of catalyst for membrane Type B and C.

Time(min)	Type B $n_{\text{reag}}/g_{\text{cat}} \times 10^3$	Type C $n_{\text{reag}}/g_{\text{cat}} \times 10^3$
0	0	0,00
20	0,74	1,04
60	2,40	1,49
80	2,54	2,04
100	2,60	2,18
120	2,65	2,25

On the other side, in the nanocomposite membranes graphene and  $\text{TiO}_2$  are strongly intersected and the graphene network could be not continuous, with a consequent low efficiency of the graphene activity.

Some informations regards the lifetime of the nanostructured membranes have been obtained by performing three photo-degradation cycles. The use of controlled feeding, by means without potential poisons for the photo-catalyst, and a proper membrane regeneration by stripping of inert gas ( $\text{N}_2$ ), resulted on the same performance in every run cycle.

As regards the effect graphene on the photocatalytic degradation, it is known from the literature that graphene and graphene oxide [30–33] can act as an electron donor or acceptor minimizing the recombination of electron–hole pairs; furthermore, thanks to their remarkable electrical transport properties, the separation of the electron–hole is increased resulting on enhanced photocatalytic performance. As regards membrane Type C, during the hydrothermal treatment of the GO, it has been found [33] that the functional groups on the surface of the GO (i.e.  $-\text{OH}$ ,  $-\text{COOH}$ , and so on) disappeared. As a consequence, some unpaired  $\pi$  electrons bonded with the free electrons on the surface  $\text{TiO}_2$  formed a  $\text{Ti}-\text{O}-\text{C}$  structure, which then shifted up the valence band edge and reduced the band gap. Even though the aforementioned reasons clarified the good performance of both the graphene based membranes, a further explanation of the better behavior of membrane Type B than Type C, has been speculated to be also related to an hinder effect by graphene to the gas adsorption on the photocatalyst surface of the nanocomposite membrane.

Looking at the graphene content, the performance of membrane Type B and Type B-2 have been reported in Fig. 11. It can be depicted that if the graphene content increased from  $0,04 \text{ mg/cm}^2$  to  $0,08 \text{ mg/cm}^2$  the photocatalytic degradation of methanol fell down dramatically to 13%. The excess amount of graphene loading overwhelmed the benefit of synergetic charge transport, resulting in a decreased efficiency. This is probably because the effect of graphene loading on the performance of the resultant composites is based on the balance between the benefit of synergetic charge transport and reduced light utilization efficiency [34]. Since

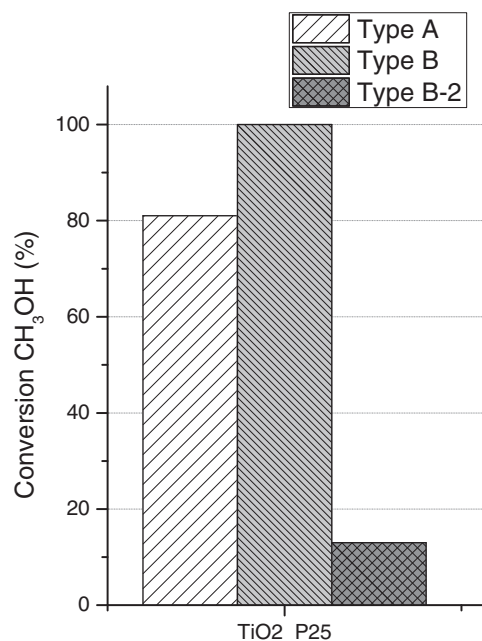


Fig. 11. Bar chart of the methanol conversion as a function of the graphene content: Type A pristine  $\text{TiO}_2$ ; Type B graphene  $0,04 \text{ mg/cm}^2$ ; Type B-2 graphene  $0,08 \text{ mg/cm}^2$ .

graphene has a strong light absorbance, its excess over a critical value, could result in a reduction of the light utilization efficiency. This behavior perfectly agrees with the literature study of Zhang et al., [26], and the results suggested a synergistic effect between the graphene and TiO<sub>2</sub> nanoparticles, by means that in order to achieve an optimal photocatalytic performance, it is crucial to control the composition ratio in the nanocomposite of TiO<sub>2</sub>-graphene.

#### 4. Conclusions

In this study nanostructured membranes based on electrospun nanofibers and TiO<sub>2</sub>-graphene photocatalyst spread over their surface were produced and characterized in two different conformations: the layer by layer and the nanocomposite ones. With respect to the membrane that contains solely TiO<sub>2</sub>, all the composite membranes showed higher photocatalytic efficiencies, which should be attributed to the synergetic charge transfer effect of the composites, as well as to a reduction of the TiO<sub>2</sub> band gap, according to the literature. It has been revealed that both the layer by layer configuration (Type B) and the nanocomposite one (Type C) led a complete photo-degradation of gas-phase methanol to CO<sub>2</sub> and water, even if with different kinetic constant. Different concentrations of co-photocatalyst were tested and it has been depicted that there is a threshold limit over which the graphene light adsorption is predominant with a consequent effect of the reduction of the light utilization efficiency of TiO<sub>2</sub>. The obtained results are promising and makes these active filter media as a good candidate in the development of advanced solutions for indoor environmental quality.

#### Appendix A. Supplementary data

Supplementary data associated with this article can be found, in the online version, at <http://dx.doi.org/10.1016/j.apcatb.2015.04.006>.

#### References

- [1] WHO guidelines for indoor air quality: selected pollutants (2010) ISBN 978 92 890 0213 4; <http://www.euro.who.int/en/health-topics/environment-and-health/air-quality/policy/who-guidelines-for-indoor-air-quality/chemical-indoor-air-pollutants-selected-pollutants-2010/who-guidelines-for-indoor-air-quality-selected-pollutants>
- [2] S. Wang, H.M. Ang, M.O. Tade, *Environ. Int.* 33 (2007) 694–705.
- [3] M. Modesti, M. Roso, C. Boaretti, S. Besco, D. Hrelja, P. Sgarbossa, A. Lorenzetti, *Appl. Catal. B-Environ.* 144 (2014) 216–222.
- [4] H. Wang, X. Yuan, Y. Wu, H. Huang, X. Peng, G. Zeng, H. Zhong, J. Liang, M.M. Ren, *Adv. Colloid Interface Sci.* 195–196 (2013) 19–40.
- [5] N.R. Khalid, E. Ahmed, Z. Hong, L. Sana, M. Ahmed, *Curr. Appl. Phys.* 13 (2013) 659–663.
- [6] H. Zhang, X. Lv, Y. Li, Y. Wang, J. Li, *ACS Nano* 4 (2010) 380–386.
- [7] C.H. Kim, B.H. Kim, K.S. Yang, *Carbon* 50 (2012) 2472–2481.
- [8] V. Štengl, S. Bakardjieva, T.M. Grygar, J. Bludská, M. Kormunda, *Chem. Cent. J.* 7 (2013) 41.
- [9] D. Wang, D. Choi, J. Li, Z. Yang, Z. Nie, R. Kou, D. Hu, C. Wang, L. Saraf, J. Zhang, *ACS Nano* 3 (2009) 907–914.
- [10] N.S. Andryushina, O.L. Stroyuk, *Appl. Catal. B-Environ.* 148–149 (2014) 543–549.
- [11] B. Qiu, M. Xing, J. Zhang, *J. Am. Chem. Soc.* 136 (2014) 5852–5855.
- [12] S. Ding, J.S. Chen, D. Luan, F.Y.C. Boey, S. Madhavi, X.W.D. Lou, *Chem. Commun.* 47 (2011) 5780.
- [13] Y. Tang, C. Lee, J. Xu, Z. Liu, Z. Chen, Z. He, Y. Cao, G. Yuan, H. Song, L. Chen, *ACS Nano* 4 (2010) 3482.
- [14] N. Yang, J. Zhai, D. Wang, Y. Chen, L. Jiang, *ACS Nano* 4 (2010) 887.
- [15] S. Sun, L. Gao, Y. Liu, Y. Appl, *Phys. Lett.* 96 (2010) 083113.
- [16] K. Demeestere, A. De Visscher, J. Dewulf, M. Van Leeuwen, H. Van Langenhove, *Appl. Catal. B- Environ.* 54 (2004) 261–274.
- [17] C.E. Welty, R.E. Wicks, *Fundamentals of Momentum, Heat and Mass Transfer*, fifth ed., John Wiley & Sons, New York, 2008.
- [18] L.M. Malard, M.A. Pimenta, G. Dresselhaus, M.S. Dresselhaus, *Phys. Rep.* 473 (2009) 51–87.
- [19] S. Gupta, E. Heintzman, J. Jasinski, *J. Raman Spectrosc.* 46 (2015) 217–230.
- [20] M.A. Pimenta, G. Dresselhaus, M.S. Dresselhaus, L.G. Cançado, A. Jorio, R. Saito, *Phys. Chem. Chem. Phys.* 9 (2007) 1276–1291.
- [21] A.C. Ferrari, J.C. Meyer, V. Scardaci, C. Casiraghi, M. Lazzeri, F. Mauri, S. Piscanec, D. Jiang, K.S. Novoselov, S. Roth, A.K. Geim, *Phys. Rev. Lett.* 97 (2006) 187401.
- [22] A.C. Ferrari, *Solid State Commun.* 143 (2006) 47–57.
- [23] H. Zhang, P. Xu, G. Du, Z. Chen, K. Oh, D. Pan, Z. Jiao, *Nano Res.* 4 (3) (2011) 274–283.
- [24] F.D. Hardcastle, *J. Ark. Acad. Sci.* 65 (2011) 43–48.
- [25] T. Szabo, O. Berkesi, P. Forgo, K. Josepovits, Y. Sanakis, D. Petridis, I. Dekany, *Chem. Mater.* 18 (2006) 2740–2749.
- [26] Y. Zhang, Z.R. Tang, X. Fu, Y.J. Xu, *ACS Nano* 4 (2010) 7303–7314.
- [27] D. Chen, A.K. Ray, *Appl. Catal. B-Environ.* 23 (1999) 143–157.
- [28] S.B. Kim, S.C. Hong, *Appl. Catal. B- Environ.* 35 (2002) 305–315.
- [29] O. Levenspiel, *Chemical Reaction Engineering*, third ed., John Wiley & Sons, New York, 1999.
- [30] A.K. Boulamanti, C.A. Korologos, C.J. Philippopoulos, *Atmos. Environ.* 42 (2008) 7844–7850.
- [31] W.-K. Jo, H.-J. Kang, *Powder Technol.* 250 (2013) 115–121.
- [32] Zhou, X. Zhang, Q. Zhang, F. Dong, F. Wang, Z. Xiong, *J. Mater. Chem. A* 2 (2014) 16623–16631.
- [33] Y. Zhang, C. Pan, *J. Mater. Sci.* 46 (2011) 2622–2626.
- [34] N. Yang, Y. Liu, H. Wen, Z. Tang, H. Zhao, Y. Li, D. Wang, *Nano* 7 (2013) 1504–1512.